

# An Analysis of DES Cluster Simulations through the IMCAT and Shapelets Weak Lensing Pipelines

M.S.S. Gill<sup>1\*</sup>, J.C. Young<sup>1</sup>, J.P. Draskovic<sup>1</sup>, K. Honscheid<sup>1</sup>, H. Lin<sup>2</sup>, N. Kuropatkin<sup>2</sup>, P. Martini<sup>1,3</sup>, M. Peeples<sup>3</sup>, E. Rozo<sup>1,4</sup>, G.N. Smith<sup>1</sup>, D.H. Weinberg<sup>1,3</sup>

<sup>1</sup> Center for Cosmology and AstroParticle Physics, The Ohio State University, Columbus, Ohio 43210, USA

<sup>2</sup> The Fermi National Accelerator Laboratory, Batavia, Illinois 60510, USA

<sup>3</sup> Department of Astronomy, The Ohio State University, Columbus, Ohio 43210, USA

<sup>4</sup> The Kavli Institute for Cosmological Physics, 5640 South Ellis Avenue, Chicago, Illinois 60637, USA

30 October 2018

## ABSTRACT

We have run two completely independent weak lensing analysis pipelines on a set of realistic simulated images of a massive galaxy cluster with a singular isothermal sphere profile (galaxy velocity dispersion  $\sigma_v = 1250$  km/sec). The suite of images was constructed using the simulation tools developed by the Dark Energy Survey. We find that both weak lensing pipelines can accurately recover the velocity dispersion of our simulated clusters, suggesting that current weak lensing tools are accurate enough for measuring the shear profile of massive clusters in upcoming large photometric surveys. We also demonstrate how choices of some cuts influence the final shear profile and  $\sigma_v$  measurement. Analogously to the STEP program, we make all of these cluster simulation images publically available for other groups to analyze through their own weak lensing pipelines.

**Key words:** Cluster Weak Lensing – Stage III Photometric Surveys – Dark Energy Survey

## 1 INTRODUCTION

Gravitational weak lensing, by both galaxy clusters and large scale structure as cosmic shear, has become one of the most promising observational avenues in recent times to place constraints on cosmological parameters and models (e.g. Albrecht et al. 2006, Peacock et al. 2006, Abbott et al. 2005). This is partly because it does not suffer from the inherent uncertainties involved in extrapolating cluster masses from other measurement techniques such as galaxy population richness class, x-ray luminosity of the hot intracluster gas, or galaxy velocity dispersion. In some sense, cluster weak lensing is the most direct measure of the total mass of a cluster, both seen and unseen. It is thus highly critical to ascertain exactly how accurate and precise the results from available current pipelines are in both the cluster and cosmic shear contexts. The cosmic shear context has especially been tested in recent years through the STEP and GREAT collaborations (Massey et al. 2007a, Heymans et al. 2005, Bridle et al. 2008), but there has been no analogous collaborative effort to verify the validity of lensing pipelines in the context of cluster weak lensing. With the public release

of the images used in this analysis, we aim to begin rectifying this in anticipation of upcoming major Stage III and Stage IV surveys (Albrecht et al. 2006), which will collect very large amounts of data useful for cluster weak lensing.

In the case of the STEP and GREAT programs, sets of simulated images were made with the aim especially of comparing and optimizing pipelines designed for the measurement of cosmic shear. For this purpose, having images with constant shear and constant Point Spread Function (PSF) across the field was sufficient for verifying several of the primary properties of the pipelines. However, for cluster weak lensing analyses we know that the shear will vary both in magnitude and direction across the field. Thus to test pipelines for applicability to cluster weak lensing analyses, it is more suitable and realistic to make simulated images which incorporate variation of both the shear and the PSF across the field. We did this by making simulated images in which an isothermal sphere shear is applied across the entire focal plane, and which further incorporate a PSF that varies linearly in anisotropy size and magnitude identically across each CCD.

One example of a major upcoming Stage III observational campaign is the Dark Energy Survey (DES) (Abbott et al. 2005), scheduled to begin taking data in the

\* Email: msgill@astronomy.ohio-state.edu

Fall of 2011. DES will use four main techniques to place constraints on Dark Energy: (1) galaxy cluster number count distributions, (2) weak lensing cosmic shear measurements, (3) galaxy angular clustering measurements, and (4) distance measurements to Type Ia supernovae. Cluster weak lensing to determine cluster masses, and other properties such as concentrations, is also one of the integral components of the DES program, and will play an important role in the calibration of the first technique in the above list.

As part of the preparation for DES, weak lensing pipelines are being thoroughly tested for accuracy on simulations before the survey begins. In addition, the DES data management pipeline and analysis tools are being extensively exercised in pre-observation DES Data Challenges with realistic images. Following from these, and using the tools developed for the Data Challenges, we constructed a set of realistic images containing a simulated galaxy cluster. We then processed these images through two completely independent weak lensing pipelines and demonstrated that the shear measurements are robust enough to reconstruct the cluster mass reliably. We also studied how different configuration and selection choices in the weak lensing pipelines affect the final cluster mass reconstruction.

We analyzed these sample cluster images with two pipelines based on publically available weak lensing codes: IMCAT – an implementation of the Kaiser, Squires, & Broadhurst (Kaiser et al. 1995) method – and Shapelets (Refregier 2003), and we present the results in this paper. It will be very useful to test multiple weak lensing pipelines on these cluster simulations, and we have made them publically available to the wider cosmological and weak lensing communities for this purpose at the following website: [<http://ccapp.osu.edu/DEScluster>].

The structure of the paper is as follows: in Section 2 we describe the simulated cluster. In Section 3 we describe the overall pipeline flow, object extraction and processing as well as test our PSF removal procedures on the simulated cluster. In Section 4 we give our results, in Section 5 we show how the results vary with certain cuts, and in Section 6 we give our conclusions.

## 2 SIMULATED CLUSTER IMAGE PROPERTIES

### 2.1 Description of Background Galaxy Properties

Several cluster images were created with the gravitational weak lensing shear determined by the Singular Isothermal Sphere (SIS) model using the tools developed by the DES simulation group. Objects in the simulated images came from the same simulated galaxy and stellar catalogs used to populate image simulations generated for the annual DES Data Challenge process, which is carried out to help develop and test DES data processing and science analysis pipelines. Specifically, the catalogs used in this paper were the ones employed for the so-called DES “Data Challenge 4,” carried out in 2008-2009.

The galaxy catalogs used the publically available Hubble Volume (Colberg et al. 2000) as the parent dark matter N-body simulation box. Specifically the  $\Lambda$ CDM Hubble Volume simulation was used, with cosmology  $\Omega_M =$

0.3,  $\Omega_\Lambda = 0.7$ ,  $h = 0.7$ ,  $\sigma_8 = 0.9$  and a light cone with redshift limit  $z = 1.4$ . Galaxies were assigned to Hubble Volume dark matter particles using the ADDGALS method (see Appendix A of Gerdes et al. 2009, Wechsler et al. 2009, Wechsler 2004), whereby each galaxy was assigned the properties of a real Sloan Digital Sky Survey (SDSS) galaxy, and the procedure reproduces the local luminosity-color-density correlations from the SDSS. ADDGALS also reproduces the magnitude-dependent 2-point function, which is important to get correct cluster color-magnitude diagrams. In particular, to populate the galaxies in the image we used the Data Challenge 4 DES mock galaxy catalog, which covers a 573 deg<sup>2</sup> subset of the Hubble Volume sky area. This galaxy catalog has a surface density of about 13 galaxies per arcmin<sup>2</sup> down to an apparent magnitude limit in the  $i$  band of about  $i = 24$ . The luminosity function model used was that of Blanton et al. (2003) for the SDSS, with simple passive luminosity evolution applied ( $M_*$  brightens by 1.3 mag per unit redshift) irrespective of galaxy type. No redshift evolution beyond the local SDSS color-environment correlations was included. Galaxies were assigned shape parameters using shapelet coefficients (Refregier 2003), where the master shapelet coefficient distribution used was derived from a set of about 18,000 galaxies in  $i$ -band CFHT MegaCam images, taken from the public Cosmic Evolution Survey (COSMOS; Scoville et al. (2007)) data set. The shapelet decompositions were carried out to order  $n=15$ , corresponding to using a total of 136 shapelet coefficients to describe each galaxy. The COSMOS/CFHT galaxies were assigned to the DES mock catalog galaxies using a simple nearest neighbor matching in the space of  $griz$  magnitudes. No size or shape evolution was included other than redshift effects due to cosmology.

The stellar catalogs were based on real USNO-B stars (Monet et al. 2003) at the bright end ( $r < 20$ ) and simulated stars at the faint end ( $r > 20$ ), with the latter derived from a web based tool employing the Besancon stellar population synthesis model for our Galaxy<sup>1</sup> to generate simulated stars.

### 2.2 Details of Cluster Simulation

The simulated cluster is located at a redshift of 0.33, with  $M_{200} = 1.5 \cdot 10^{15} M_\odot$ ,  $r_{200} = 1$  Mpc and  $\sigma_v = 1250$  km/sec, where  $M_{200}$  ( $r_{200}$ ) is the mass (radius) out to a distance within which the average overdensity is 200 times the critical density of the universe at that redshift and  $\sigma_v$  is the velocity dispersion for an SIS profile (see Sec. 4.1 and for details on SIS properties see e.g. Sec. 3.1 of Narayan & Bartelmann (1996)). In order to avoid the strong lensing regime within the Einstein radius, which for this cluster for sources at  $z = 1$  is about 27" (see Sec. 4.1), the shear is set to zero for objects within a certain radius. To be conservative we choose the value of this radius by excluding the region where objects would have tangential shear  $\gamma_t > 0.2$  in the limit of  $z \rightarrow \infty$ , which corresponds to the area within a radius of about 100" from the cluster center. Using the pixel scale of the Dark Energy Camera (DECam) of 0.27 arcseconds per pixel (Honscheid et al. 2008), this corresponds to being within about 400 pixels from the cluster center. Except for

<sup>1</sup> <http://model.obs-besancon.fr/>

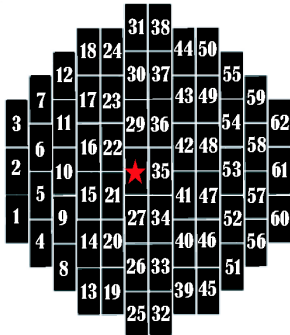


**Figure 1.** A graphical representation of the image plane with the standard DES CCD numbering. The red star marks the cluster center.

this region, galaxy objects have SIS shear assigned accordingly across the full 3 square degree image mosaic. To get some sense of the scale of the shear variation, for a source at  $z = 1$  the shear falls to about  $\gamma = 0.02$ , at a radius of  $20'$  (6 Mpc) from the cluster center, roughly one third of the image plane radius.

Each galaxy object generated according to this prescription has five magnitudes in the SDSS-like filters  $g, r, i, z$  and  $y$ , as well as an assigned redshift, which are all contained in truth catalog files. Seven image files were produced with varying levels of complexity, and their properties are summarized in Table 1. Partial images for five of the files are shown in Fig. 2. In order to test how the pipelines vary for differing noise levels, there are three levels of noise included in the simulated images: No Noise, LN (Low Noise) and HN (High Noise). The LN images are what would be seen by DES with a 600 s exposure with readout and object photon noise included but without sky noise. The effects of the sky noise are present in the HN images which have a 13 times higher noise level. Our HN images should be fairly similar to nominal DES exposures which will be 100 seconds long with 5 passes throughout the survey.

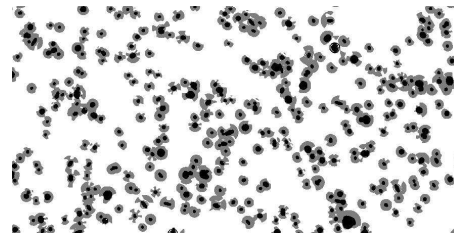
### 2.3 Description of Simulated Images

The DES focal plane consists of 62 imaging CCDs, each with  $x(y)$  dimensions of 2048 (4096) pixels. The image plane is shown in Fig. 1. Since the pixel scale of the DECam is 0.27 arcseconds per pixel, the radius of the image plane is  $\sim 65$  arcminutes, and the field of view is  $\sim 3$  square degrees.

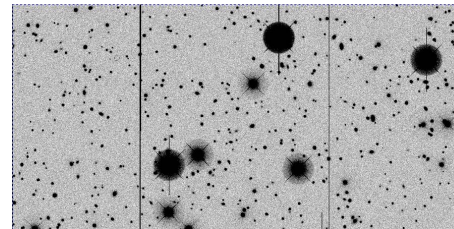
The truth catalog contains many pieces of information about each object, the most useful for our purposes being:

- (RA, DEC) and  $(x, y)$  pixel positions,
- whether the object is a star or a galaxy,
- redshift,
- $g, r, i, z, y$  magnitudes,
- SIS shear

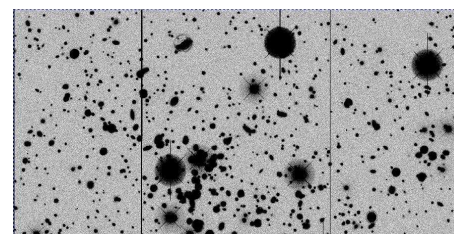
For simplicity, the images were made only in the  $r$ -band, but as noted above, the truth catalog contains the magnitudes for four other bands for each object, which are assigned according to the prescription described in Sec. 2.1. To apply the shear from the cluster, the exact SIS value for a given



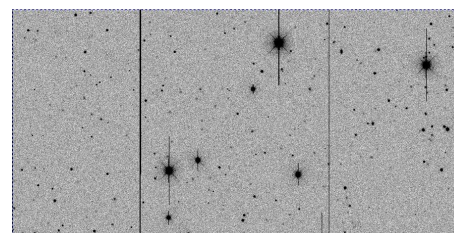
(a) Original file – no noise



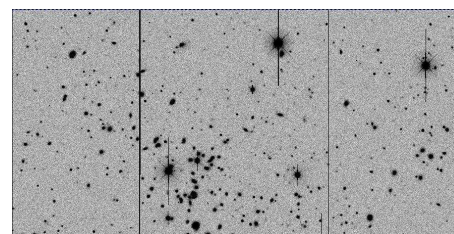
(b) Low noise file - without foreground galaxies



(c) Low noise file - with foreground galaxies



(d) High noise file - without foreground galaxies



(e) High noise file - with foreground galaxies

**Figure 2.** Partial focal plane images from the simulated cluster, for the portion containing the cluster, with size about 1000 pixels high, and 2000 pixels across. Background galaxies are visible as well as clear diffraction spikes (from the DECam telescope assembly) on the saturated foreground stars in the four images that contain them, and foreground cluster galaxies in the two images that contain them. It is clear that many more objects are seen in the low noise files. The vertical lines running from top to bottom in all four images with noise are bad CCD columns.

**Table 1.** Brief description of the simulated images.

File Description	Noise	Shear	Included Objects
Original Non-sheared	None	None	Background Galaxies
Sheared	None	Cluster Shear	Background Galaxies
High Noise	High	Cluster Shear	Background Galaxies
High Noise + PSF Applied	High	Cluster Shear + PSF	Background Galaxies Stars
High Noise + PSF Applied + Foreground Galaxies	High	Cluster Shear + PSF	Background Galaxies Stars Foreground Galaxies
Low Noise + PSF Applied	Low	Cluster Shear + PSF	Background Galaxies Stars
Low Noise + PSF Applied + Foreground Galaxies	Low	Cluster Shear + PSF	Background Galaxies Stars Foreground Galaxies

**Table 2.** Rounded initial numbers of objects in the labelled column categories of Table 1, all in thousands. No cut has been applied to the files with foreground galaxies, so all of these are included in the yield for Galaxy Objects. 100k galaxies across the DES focal plane would correspond to about 9 galaxies per square arcminute.

File	Raw Objects (thousands)	Cleaned Objects (thousands)	Stellar Objects (thousands)	Galaxy Objects (thousands)
Original	105	28	n/a	28
Sheared	105	28	n/a	28
High Noise	46	44	n/a	44
HN+PSF	59	52	11	26
HN+PSF+ Foreground	74	66	11	40
Low Noise+PSF	128	105	14	78
LN +PSF+ Foreground	146	115	14	89

location in the image plane is convolved with the intrinsic object ellipticity through the Shapelets shear convolution algorithm (Refregier 2003). For simplicity, magnification from the cluster was *not* accounted for in the images.

To make the cluster simulation more realistic, five of the seven images incorporate a PSF that affects all the objects in the image. This PSF varies in ellipticity and size across each CCD, but it has an identical form for all 62 CCDs. The PSF is modeled with two pieces: the first is an isotropic Gaussian-smearing function with a slowly linearly increasing width varying in 10 equally spaced steps, each of about 0.02 pixels. In total, the width varies from 2.9 pixels at the bottom to 3.1 pixels at the top of the CCD. The second piece of the PSF is an anisotropic component whose total ellipticity linearly decreases in the same 10 steps from the bottom to the top of each CCD. In total, this ellipticity varies from 0.6% at the bottom to 0.2% at the top of the CCD.

Fig. 3a shows the average of the two components of ellipticities for the image-selected stars in linear strips in each CCD. The inclination of each line segments indicates the direction of the average ellipticity, and the length indicates

its magnitude. It can be seen that the magnitude of the ellipticity becomes steadily smaller towards the top of the CCD. In Fig. 3b we plot the average of a linear function of the full width at half maximum (FWHM) for the image-selected stars in a grid on each CCD. Here, the radius of each circle indicates the scaled FWHM magnitude for that strip. It can be seen that towards the top of the CCD the FWHM becomes steadily larger.

### 3 PROCESSING THROUGH THE PIPELINES

#### 3.1 Overview

In order to process a set of either simulated or real images and extract either a final cluster mass measurement or the SIS velocity dispersion  $\sigma_v$ , there are five fairly distinct steps that must be executed:

- (i) Find objects in the image and build a catalog of their properties.

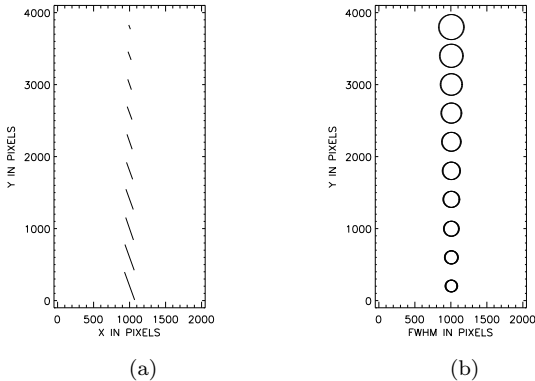


**Figure 3.** (a) Average of SExtractor ellipticities in horizontal strips in each CCD (the PSF pattern is identical for all CCDs), with the inclination of the segment indicating the direction of the average, and the length indicating its magnitude. (b) Average of the FWHM in cells in the same strips, with the radius of the circle indicating the scaled FWHM magnitude; specifically, with values chosen to make the variation visible:  $\frac{(FWHM)-2.8}{3.2} \times 1000$  (See Sec. 2.3).

- (ii) Use these properties to determine which of the objects are stars and which are galaxies.
- (iii) Use the objects determined to be stars to measure the PSF and remove its effect on the lensed galaxies.
- (iv) Refine galaxy selection with cuts that attempt to pick only galaxies behind the cluster.
- (v) Use the shear measurements to reconstruct a shear profile of the cluster and infer its mass or velocity dispersion.

We detail these steps in the following sections.

### 3.2 Source Extraction

As the first step in both the IMCAT and Shapelets pipeline, we execute Step (i) of Sec. 3.1 and extract objects from the image files using Source Extractor (or “SExtractor”, Bertin & Arnouts 1996). SExtractor runs over an image and builds a catalog of objects that contains various properties. Though the two pipelines invoke SExtractor in different ways, we use identical parameters in their respective configuration files and thus obtain fully identical SExtractor object catalogs from them with respect to the number of objects yielded and their properties. Our SExtractor configuration files are available on the website.

### 3.3 Star Selection

We next move to Step (ii) of Sec. 3.1, separating star and galaxy objects in the SExtractor object catalogs. Even though the star objects are very clear in this simulated cluster, it is useful to verify our star selection tools, which are needed for real images.

It is very important to have a good selection of stars when classifying objects because this determines the shape of the PSF that is later removed. Thus, we developed a number of tests to find the best sample of stars for our PSF determination. In general, stars are selected from an image by plotting the magnitude of the object vs. a measure of size

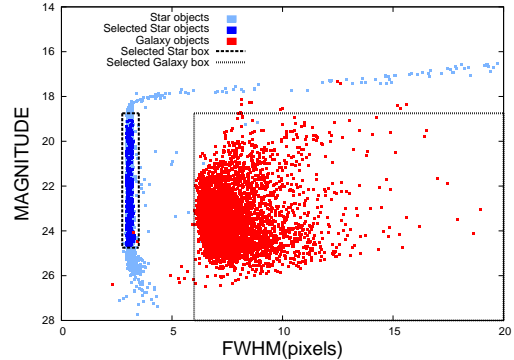


**Figure 4.** Magnitude ( $r$ -band) vs. FWHM (in pixels) for the LN image with noise, PSF, and foreground objects. Colors indicate the star and galaxy objects – stars in blue, and galaxies in red. Only 10% of the objects are shown for clarity.

such as the FWHM, and then selecting out the stellar locus in this figure, which is defined by objects that are small and fall in a very narrow range of sizes but a wide range of magnitudes. The FWHM is a standard output from SExtractor obtained by fitting the object with a Gaussian profile (see Sec. 8.4.4 of Holwerda 2005). The magnitude measure we chose to use from SExtractor, the MAG\_AUTO output, is obtained by fitting the object to an elliptical aperture using second-order moments of its brightness (see Sec. 7.4 of Holwerda 2005).

In Fig. 4, we plot the magnitude vs. FWHM of objects in the LN image with noise, PSF, and foreground objects. In blue are objects that are known from the truth catalog to be stars, and in red are the “truth-matched” galaxies. We see clearly there the stellar locus, or “star column”, indicated by the objects contained in the vertical box on the left. Specifically, to isolate the “good star” objects we chose a FWHM of 2.9 to 3.3 pixels and a magnitude from 20.3 to 26. In the same figure we see several regions of stars, starting from the top arm stretching to the right: these are saturated stars which are not useful for PSF estimation. Moving down, we see in the vertical box in dark blue the good stars that are selected for the PSF shape estimation, and then in the region below this rectangular box stars that are dim and have poorly measured shapes, which we discard.

To make the initial selection of the galaxies, we use the information that they are generally larger than the stars in the number of pixels they cover, and have less surface brightness per pixel. They are thus generally characterized by larger FWHMs and fainter apparent magnitudes and they are the red objects on the right in Fig. 4. The magnitude limit we have chosen is approximately 26.5, though realistic  $r$ -band limits in DES will be closer to 24. The dimmer galaxies are in our sample mostly because the initial catalog we are working with has an  $i$ -band magnitude limit of approximately 24, but an attempt was made to make realistic color distributions, which resulted in fainter magnitudes in the  $r$ -band (see Sec. 2.1). We also note in the figure that there is a fairly sharp edge for the smallest galaxies. This is caused by a discrete lower cutoff in the size of the galaxies that were included in the simulation.

### 3.4 Galaxy Shape Estimators and PSF Removal

Moving next to Step (iii) of Sec. 3.1, we briefly describe the estimators the two pipelines use for the shapes of the galaxies, and the mechanisms by which they remove the PSF from the image, beginning with some formalism that is common to both pipelines.

#### 3.4.1 Common Formalism for Shape Estimation

The initial steps are to take the first moments of the image intensity of the object as a function of pixel position  $I(x, y)$ , to find its center, then the second (quadrupole) moments which will be needed to extract the ellipticity (e.g. Bridle et al. 2008).

To form the first moments of the image  $I(x, y)$ , we define

$$\bar{x} = \int I(x, y) x \, dx \, dy, \quad (1)$$

$$\bar{y} = \int I(x, y) y \, dx \, dy \quad (2)$$

and for the quadrupole moments we define

$$Q_{xx} = \int I(x, y) (x - \bar{x})^2 \, dx \, dy, \quad (3)$$

$$Q_{xy} = \int I(x, y) (x - \bar{x})(y - \bar{y}) \, dx \, dy, \quad (4)$$

$$Q_{yy} = \int I(x, y) (y - \bar{y})^2 \, dx \, dy. \quad (5)$$

Next, the ellipticity components  $e_1$  and  $e_2$  may be extracted by forming from the second moments the complex quantity

$$e = \frac{Q_{xx} - Q_{yy} + 2iQ_{xy}}{Q_{xx} + Q_{yy} + 2(Q_{xx}Q_{yy} - Q_{xy}^2)^{1/2}} \equiv e_1 + ie_2. \quad (6)$$

For an object with constant ellipticity isophotes having major axis  $a$  and minor axis  $b$  and orientation of the major axis  $\theta$  with respect to the positive x-axis (see Fig. 5), the two components of the ellipticity from eq. 6 become

$$e_1 = \frac{a-b}{a+b} \cos 2\theta, \quad (7)$$

$$e_2 = \frac{a-b}{a+b} \sin 2\theta. \quad (8)$$

Gravitational lensing maps the unlensed image, specified by coordinates  $(x_u, y_u)$ , to the lensed image  $(x_\ell, y_\ell)$  using a matrix transformation:

$$\begin{pmatrix} x_\ell \\ y_\ell \end{pmatrix} = \mathcal{A} \begin{pmatrix} x_u \\ y_u \end{pmatrix} \quad (9)$$

where  $\mathcal{A}$  is the shear matrix:

$$\mathcal{A} = \begin{pmatrix} 1 - g_1 & -g_2 \\ -g_2 & 1 + g_1 \end{pmatrix} \quad (10)$$

and  $g_1, g_2$  are the two components of reduced shear

$$g = \frac{\gamma}{1 - \kappa} \quad (11)$$

where  $g$  simply becomes the normal shear  $\gamma$  in the limit of the convergence  $\kappa \rightarrow 0$ , which generally holds in the weak

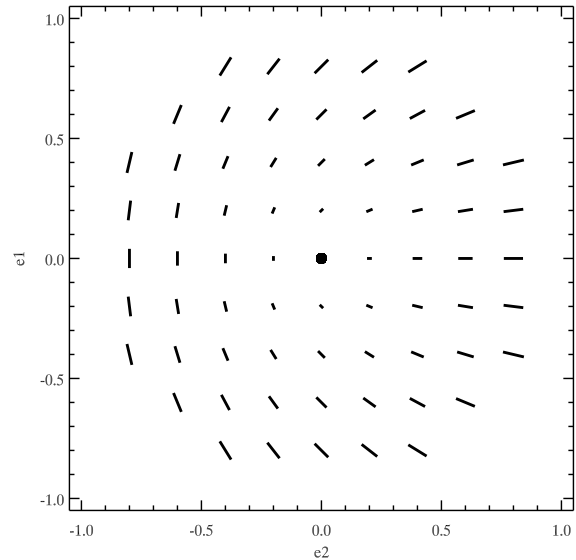


**Figure 5.** Representation of object ellipticity representation with length indicating magnitude and angle indicating direction, using the parameterization in the two quantities  $e_1$  and  $e_2$  (see eqs.7-8). Note how, due to its rotational symmetry, rotating any ellipse by  $\pi$  yields the same  $e_1$  and  $e_2$  parameters.

lensing regime for clusters, and will be assumed henceforth here.

The intrinsic ellipticity of a galaxy  $e$  transforms under shear as

$$e^\ell = \frac{e^i - g}{1 - g^* e^i}, \quad (12)$$

where  $e^\ell$  is the observed sheared (lensed) shape of the galaxy. For  $|g| < 1$  this quantity can be Taylor-expanded to give

$$\langle e^i \rangle \simeq g \quad (13)$$

to first order in  $g$ , where we have assumed  $\langle e_1^i \rangle = \langle e_2^i \rangle = 0$  and the average is over a population of galaxies. Thus, an average of the tangential component of the shear (the ‘E-mode’) over a population of galaxies in an annulus around the cluster center will yield an estimate of the shear in that annulus, which is a fact we shall use later in our cluster profile shear extraction in Sec. 4. The average of the component tilted at  $\frac{\pi}{4}$  relative to the tangential component is the ‘B-mode’ and should be exactly zero for the case of perfect cluster shear (see e.g. Sec. 4 of Bartelmann & Schneider 2001 or Bernstein & Jarvis 2002).

#### 3.4.2 Shapelets PSF Removal

To execute the Shapelets PSF removal pipeline, after selecting out the star objects, we form an initial shapelet model for each of them. Then we pick an optimal fixed interpolation order and Gaussian basis function width common for all of these stars and form a shapelet model for each one. The choice of order and width that one uses will influence the ellipticity of the shapelet objects. To determine the optimal order and width for the decomposition, Shapelets uses a  $\chi^2$ -minimization algorithm to determine the best match

between the reconstructed and original images. After all of the stars have been decomposed down to a shapelet model with a fixed order and width, we determine the order of the fitting function to interpolate each of the shapelet coefficients across the image plane and construct the PSF model. This constructed PSF is then used to remove the effects of the PSF shear from the galaxy objects. In Shapelets it is possible to estimate the final shape of a galaxy in a number of ways, in this paper we use the minimal estimator, which is a ratio formed from three of the low order shapelet coefficients, specifically

$$\gamma_{\text{sh}} \equiv \frac{\sqrt{2}f_{22}}{f_{00} - f_{40}}, \quad (14)$$

(see e.g. eq. (39) of Massey et al. 2007b).

### 3.4.3 IMCAT PSF Removal

IMCAT also uses stars to remove the PSF-induced alteration of the size and ellipticity on the galaxy objects, relying on just quadrupole moment shape measurement rather than the entire decomposition of the shape into basis functions of an orthogonal set. It relies on the well-tested KSB algorithm (Kaiser et al. 1995) which assumes the PSF can be broken into two parts, an anisotropic and an isotropic piece, and can be removed in two steps. We first remove the anisotropic part by writing the true ellipticity of an object that would be seen without any PSF effects as

$$e_{\xi}^t = e_{\xi}^{obs} - P_{\xi\zeta}^{\text{sm}} p_{\zeta}, \quad (15)$$

where  $e_{\xi}^t$  is the vector representing the true ellipticity before PSF effects,  $e_{\xi}^{obs}$  is the observed ellipticity vector, and  $P_{\xi\zeta}^{\text{sm}}$  is called the “smear polarizability tensor”. This quantity represents the anisotropic part of the PSF, while  $p_{\zeta}$  represents the anisotropy kernel at a specific location in the image plane. We estimate  $p_{\zeta}$  by saying that stars should appear perfectly circular before PSF smearing, and thus

$$e_{\xi}^{t*} = 0 = e_{\xi}^{obs*} - P_{\xi\zeta}^{\text{sm}*} p_{\zeta}^*, \quad (16)$$

where the asterisk superscript indicates this equation holds for stars. Solving for  $p_{\zeta}^*$ ,

$$p_{\zeta}^* = (P_{\xi\zeta}^{\text{sm},*})_{\xi\zeta}^{-1} e_{\xi}^{obs*} \quad (17)$$

and a bi-polynomial interpolation is used across the image plane to estimate  $P_{\xi\zeta}^{\text{sm}}$  and  $p_{\zeta}$  at the location of the galaxies. For each galaxy

$$e_{\xi}^{t,g} = e_{\xi}^{obs,g} - P_{\xi\zeta}^{\text{sm}} \left( (P_{\xi\zeta}^{\text{sm},*})_{\xi\zeta}^{-1} e_{\xi}^{obs*} \right). \quad (18)$$

The next step is to remove the isotropic piece of the PSF and extract the shear via

$$\gamma_{\zeta} = (P^{\gamma})_{\xi\zeta}^{-1} e_{\xi}^{t,g} \quad (19)$$

where

$$P_{\xi\zeta}^{\gamma} = P_{\xi\zeta}^{\text{sh}} - \left( P_{\xi\zeta}^{\text{sm}} (P_{\xi\zeta}^{\text{sm},*})_{\xi\zeta}^{-1} P_{\xi\zeta}^{\text{sh}*} \right) \quad (20)$$

and is referred to as the “pre-seeing shear polarizability” in the literature (originally by Luppino & Kaiser 1998). Here  $P_{\xi\zeta}^{\text{sh}}$  is the “shear polarizability tensor” and encodes the information about the variation of the isotropic piece of the PSF across the plane (see Hoekstra et al. (2008) for details of the derivation of  $P_{\xi\zeta}^{\gamma}$ ).

**Table 3.** Average stellar ellipticities and their widths before and after PSF-removal stars on stars test (see Sec. 3.5).

File	$\langle e_1 \rangle$	$\langle e_2 \rangle$	$\sigma_{e_1}$	$\sigma_{e_2}$
Before PSF removal	-0.0132	-0.0110	0.0121	0.0112
After PSF removal	0.0008	0.0009	0.0095	0.0082

It has been found that the off-diagonal elements of  $P_{\xi\zeta}^{\text{sm}}$  and  $P_{\xi\zeta}^{\text{sh}}$  are close to zero, and the diagonal elements are comparable, so each of them can be approximated as the average of their trace multiplied by the identity matrix (see e.g. Sec. 4.2 of Bacon et al. 2001). This approximation makes inverting the matrices extremely rapid, has worked remarkably well in common usage, and is the implementation of KSB that we used.

### 3.5 PSF Removal Test

In order to test how well we are removing the PSF, we implemented a test that we refer to as a ‘stars on stars’ test. Here we randomly selected half of the stars to calculate the PSF distortion and apply this correction to the other half of the stars. In general, the size of the corrected stars in such a test should become smaller and the ellipticities of these stars should shrink substantially.

Because a linear variation in ellipticity and size of the stars was put into the PSF, we expect that a linear order interpolation of the PSF will be sufficient to adequately describe the PSF across each CCD. This is indeed what we find; numerically, after a linear order PSF correction, taking the 200–300 stars per CCD on the files and dividing them into two groups, we find the values in Table 3 for the average and width of the values of the ellipticities of the PSF-corrected stars. These results indicate a reduction by between one and two orders of magnitude in the average of each component of the ellipticity, and a reduction by about a third in the ellipticity width distribution.

We also did this at several other orders of the PSF functional interpolation polynomial. As one would expect, at zeroth order (constant stellar ellipticity and size assumed across whole plane), we found that in fact the average ellipticities were of the same order as before correction, and the widths barely shifted. Above order one, there was no significant reduction in either the average ellipticities nor widths above that already gained by the order one PSF removal. This confirms that a first order interpolation is sufficient to describe the PSF variation across the CCD. Of course, higher order interpolation is in general needed for real images, which will not have such a simple PSF structure or variation with spatial position.

## 4 RESULTS

Having discussed our methods and tests, we now move to the results from running both pipelines on the simulations.

#### 4.1 Fitting SIS Profiles

For an SIS cluster, the critical Einstein radius for each background galaxy is

$$\theta_E = \left( \frac{4\pi\sigma_v^2}{c^2} \right) \beta \quad (21)$$

where  $\sigma_v$  is the intrinsic three-dimensional lensing cluster galaxy velocity dispersion, and

$$\beta \equiv \frac{D_{ls}(z_l, z_s)}{D_s(z_s)}, \quad (22)$$

where  $D_{ls}(z_l, z_s)$  is the angular diameter distance from the lens to this background source galaxy, and  $D_s(z_s)$  is the distance from the observer to the background galaxy (see e.g. Bartelmann & Schneider (2001), Sec. 3.1.5). This is the radius within which the projected average surface mass density is exactly equal to the critical value of

$$\Sigma_{cr} = \frac{c^2}{4\pi G} \frac{D_{ls}(z_l, z_s)}{D_l(z_l)D_s(z_s)} \quad (23)$$

and within which strong lensing arcs may potentially be seen. The shear from a cluster on a given background galaxy depends on the Einstein radius simply as

$$\gamma(\theta) = \frac{\theta_E}{2\theta}. \quad (24)$$

Eq. 24 is the shear of any observed galaxy, and because of the distance ratio  $\frac{D_{ls}(z_l, z_s)}{D_s(z_s)}$  in the Einstein angle, a galaxy at the same radial distance from the center of the cluster but at a different background redshift is sheared differently. However, if the exact redshift for a specific lensed galaxy and thus its distance ratio factor is known, we may divide through by this and remove this variation. This results in the infinite redshift limit shear value, which is a unique function of the radial distance from the cluster center

$$\gamma_\infty(\theta) = \frac{\theta_E}{2\theta} \beta^{-1}. \quad (25)$$

This is exactly the shear that a galaxy at  $z \rightarrow \infty$  experiences, since  $\beta \rightarrow 1$  as  $z \rightarrow \infty$ . As an example, for a galaxy at  $z = 1$ , at  $1.8'$  ( $108''$ , or 400 pixels) from the cluster center, which is the radius of maximal distortion put into the simulation (see Sec. 2.2), the observed shear evaluates to about 0.12. Dividing by  $\beta$ , this becomes the infinite redshift shear value of about 0.21. It then falls steadily with radius, as can be seen by the solid red curve in Fig. 6b.

Following from eq. 25, if we fit the simple function of a hyperbola

$$f(\theta) = \frac{\xi}{\theta} \quad (26)$$

to the infinite redshift shear values, we can solve the equation

$$\xi = \frac{\theta_E}{2} \quad (27)$$

for  $\sigma_v$ :

$$\sigma_v = \sqrt{\frac{\xi c^2}{2\pi}}. \quad (28)$$

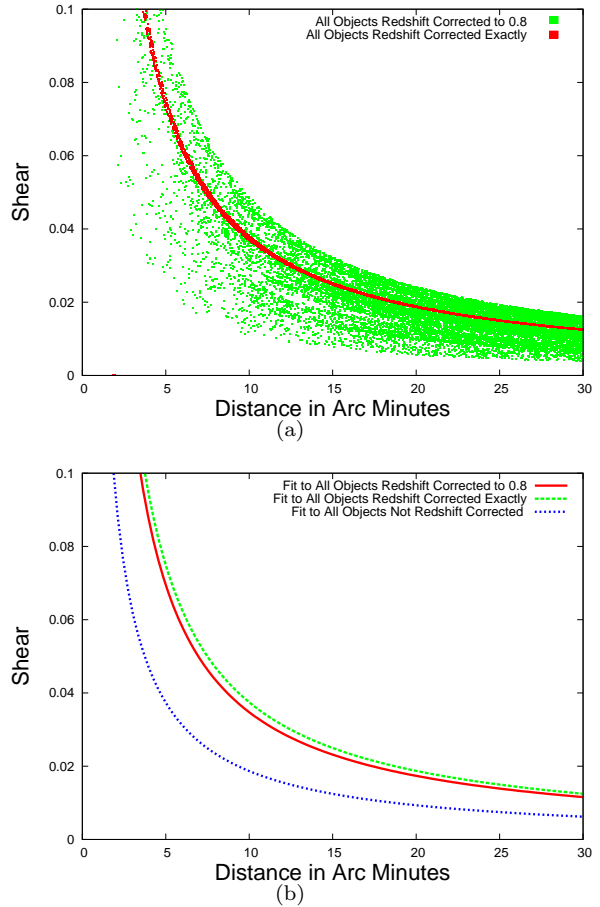


**Figure 6.** Truth shear profiles for the inner half of the image plane (to see more inner profile detail) plotted against distance from the center of the cluster in arcminutes ( $1' = 222.2$  pixels = 283 kpc for the cluster distance of  $z = 0.33$  and a flat  $\Lambda$ CDM geometry). Points labelled “Redshift Corrected Exactly” are corrected point by point by the known redshift, points labelled “Redshift Corrected to 0.84” are each corrected assuming the single sheet approximation, i.e. that each galaxy lies at  $z = 0.8$ , which is the average of the redshifts of the background galaxies. In (b) lines are unbinned fits to the three sets of points.

#### 4.2 Fits to truth shear values

We first apply the above to the truth file shear values. In this case, the shear is written into the truth file as it would be actually observed (i.e. as eq. 24, not eq. 25), so the distance ratio factor must be corrected for each object so that we can use eqs. (26-28). We may do this in two different ways and compare the results: (a) correcting point by point by the known redshift, since we know its value for each object in our simulated images (b) correcting approximately by assuming each galaxy lies at the average of the redshifts of all the background galaxies, i.e., the “single sheet approximation”. The latter is the approach most often taken in weak lensing work, since often neither the spectroscopic nor photometric redshift of each galaxy is available.

In Fig. 6 we show the results of doing the corrections in the two ways, first in Fig. 6a by plotting the E-mode data point results (see Sec. 3.4.1), and in Fig. 6b the fit profiles as functions of the distance from the center of the cluster image



**Table 4.** Table of the  $\sigma_v$  values derived from the truth file with varying forms for the redshift correction for each galaxy.

Redshift correction for each galaxy	$\sigma_v$ (km/sec)
$z = \text{Infinity}$	880
$z = 0.84$	1200
$z = \text{Exact}$	1249

to the edge of the image field. We also plot in Fig. 6b the fit profile result for the “redshift-uncorrected” results (i.e. assuming incorrectly that each galaxy is located at infinite redshift).

For all truth fit results, we use a simple least squares fitting algorithm to the unbinned points to avoid losing information in binning data, but will present also binned data for visual comparisons. Here, the unbinned fit on the exactly corrected points yields effectively the input value  $\sigma_v = 1249$  km/sec, and on all objects redshift corrected to 0.8 yields  $\sigma_v = 1200$  km/sec. Both these results have negligible error bars ( $< 1$  km/sec) since we are working with the truth values of the shear, which have no shape error (see Sec. 4.3.1 for a discussion on where the dominant error in  $\sigma_v$  arises from). As can be seen in Table 4, the exact correction results in a  $\sigma_v$  value very near the input, while the the single sheet approximation is quite far off in this case. However, this case has unrealistically small error bars, and we will see that in general in actual realistic samples, the extracted  $\sigma_v$  value falls within the one-sigma error bar of the input value.

Doing no redshift correction (fitting only the redshift-uncorrected values) results in  $\sigma_v = 880$  km/sec, again with small error bars. The lower value is obtained since we are dividing each galaxy shape simply by unity, instead of the factor  $D_{ls}(z_l, z_s)/D_s(z_s)$ , which is always less than unity. Doing no redshift correction is exactly equivalent to assuming all background galaxies are infinitely far away, which is clearly not a very good assumption for lensing.

These values are summarized in Table 4.

### 4.3 Fitting Simulated Data

We now do the fits to data sets that come out of the simulation images themselves.

#### 4.3.1 Fitting SExtractor Files

First, we fit the SExtractor data beginning with the Sheared and the Original files before any noise or PSF is added, then proceed to the file with noise, then that with PSF, and then to the final file with noise, PSF *and* the foreground galaxies present. Though this exercise is not useful in the real world because we can never get access to an image without a PSF or noise, it is instructive to do it here and see just how much these complexities dilute the pure original shear signal. In this study we are using only information from SExtractor without invoking either of the two lensing pipelines and thus with no PSF correction. That is, the shear in any given radial

bin is computed simply by using the observed ellipticity of that galaxy as computed by SExtractor vs. doing any PSF-removal processing through the pipelines.

In each case, we have corrected the shear for the redshift using the single sheet approximation and setting all the background galaxies to be at the average of the redshifts of all the background galaxies (see Sec. 4.1 for an explanation of this, and see Sec. 5.1 for a study on results from varying the type of redshift correction). We find this value by doing a match of the objects with the truth catalog, obtaining the redshift of each object, then taking the average of these redshifts. We present the  $\sigma_v$  results in this way because we found that they were similar to those we obtained by fitting to the exact redshift of each object, and correspond to what is done more commonly in lensing analyses. We now see that with realistic errors, the extracted  $\sigma_v$  value falls within the one-sigma error bar of the input value.

Table 5 lists the numerical values of our results, and Fig. 7 shows the E- and B-mode profiles averaged in 20 annular bins from the center of the cluster to the edge of the image, compared to the input shear value. The error bars shown are the one-sigma standard deviation spread in ellipticities for all the objects in that annular bin scaled by  $1/\sqrt{N}$ , where  $N$  is the number of objects in that annular bin. Since galaxies have an intrinsic shape dispersion of about  $\sim 0.3$ , this is the dominant source of statistical error, and is reduced by  $1/\sqrt{N}$  as more galaxies are collected per bin. We verified this scaling in the final fit values also by varying the number of galaxies we used in our fits, confirming that the error in the fit values followed a  $1/\sqrt{N}$  scaling.

We conclude from the results in Table 5 that, quite as we would expect, the SExtractor fits work best for the perfect sheared-only file, and every additional level of complexity moves the fit value further from the input value. It is interesting to note that in this case, the addition of foreground galaxies seems to have a greater effect on the result than even the application of the PSF.

#### 4.3.2 Fitting PSF-removed Files

We now move to the core of the lensing pipelines, the results for the files with a PSF after we have processed them through each pipeline and removed the effect of the PSF. In both IMCAT and Shapelets we use first order polynomial fits to describe the PSF-variation across the CCD, since this is the form of the PSF we initially applied to the image.

We did tests correcting galaxies for the extracted PSF in three different ways: (1) by extracting the PSF from a fit to the stars in each CCD separately, as would typically be done with real data; (2) by grouping stars from all CCDs with their relative position on that CCD into one “super” CCD and extracting the PSF from a fit to the stars in the super-CCD; (3) by extracting the PSF from a fit to 10 ‘truth stars’. These ‘truth stars’ are extracted from an image we constructed with one star in each of the 10 discrete y-positions on the CCD, each affected by the PSF for that specific y-position.

We found that the profile results changed very little whichever way we extracted the PSF, which is reasonable in this simulation because the PSF is replicated for each CCD, and because we found that the SExtracted stellar properties are such a close match to the truth star ones. Thus, we chose

**Table 5.** Table of the  $\sigma_v$  values derived from the SExtractor ellipticities. The “deviation” is the number of  $\sigma$  that the result is away from the input value of  $\sigma_v = 1250$  km/sec, i.e.  $\sigma = \frac{\text{result} - \text{input}}{\sigma_{\sigma_v}}$ . The non-sheared file doesn’t have an input  $\sigma_v$ , so the  $\sigma$  deviation is not applicable. Note that as the files progressively have noise, PSF, and foreground objects added, the deviation from the input becomes greater, and the error bars on the fit become larger, both of which we would expect since no PSF removal or foreground galaxy removal has yet been performed on these files. Note foreground *stars* have been removed in all the files which contain them – all four files with PSF and foreground galaxies – by keeping only objects with FWHM > 5 pixels and Magnitude > 20.

File	Redshift	$\sigma_v$ (km/s)	$\sigma_{\sigma_v}$ (km/s)	Deviation
Original (non-sheared) File	0.84	$\sim 0$	123	n/a
Sheared File	0.84	1223	33	0.8
High Noise File	0.64	1135	61	1.9
High Noise PSF Applied File	0.64	1051	78	2.5
High Noise Foreground Galaxies Added File	0.64	730	80	6.5
Low Noise PSF Applied File	0.84	954	26	11.4
Low Noise Foreground Galaxies File	0.84	830	31	13.7

to remove the PSF in the way closest to how it would be done in the real world, namely by extracting the PSF from a fit to the stars in each CCD. In future simulated images, we will more realistically vary the PSF across the entire focal plane. This is the plan for Data Challenge 5 for DES, scheduled to begin in Autumn 2009.

Though we will show results from all the files with a PSF, we choose the Low Noise file with foreground galaxies as our primary reference file, because it has several of the major realistic features – i.e. a PSF, foreground stars and galaxies – and can be processed through both of our pipelines. However, it does have low noise relative to the expected DES exposures (see Sec. 2.2). We expect from the values in Table 5 that this will cause it to have a smaller error in the output  $\sigma_v$  than the corresponding high noise version, which we examine quantitatively in Sec. 5.2.3.

After removing the PSF, we make a cut of  $|(\gamma_1, \gamma_2)| < 2$  on each of the resulting two components of shear for each galaxy as is regularly done in lensing pipelines<sup>2</sup>. Further, though we made the initial galaxy cut to remove stars, we next refine our selection by making a color cut of  $r - i > 0.7$  (see Sec. 5.2.1) to remove all the foreground galaxies. We choose initially to redshift-correct all objects using the single sheet approximation (see Sec. 4.1), since this is the most common practice in lensing analyses, but in Sec. 5.1 we will study how the results vary with changing this assumption. In Table 6 we show the results of this analysis on this file, compared to doing the same fit on only the SExtractor ellipticities of the objects, and we see that though the error bars have gone up by a factor of 2-3 from the SExtractor case, more significantly, the central value from each pipeline is now within one sigma of the input, where it was nearly 10 sigma away before. The error bars become larger essentially because, as part of the PSF-removal process in each

pipeline, the step of dividing by an often small polarizability increases the intrinsic shape error of each galaxy. This behavior is seen in all lensing pipelines.

The results in Table 6 are shown for 49k objects that have been position-matched between the final IMCAT and Shapelets catalogs (and the truth catalog, to make the color cut to keep background galaxies). Another way to do this comparison is by only matching each of the catalogs to the truth catalog so that the color cut to keep background galaxies can be made, but not matching the objects in each pipeline with one another, and the results for these fits are shown in the last two lines of the same table.

In Fig. 8 we show the E- and B-mode binned profiles corresponding to the results in Table 6 and compared again to the input shear. It is clearly seen that in the innermost bins, the Shapelets shear is above the input, and the IMCAT shear lies below the input, which is what leads to the  $\sigma_v$  values of Table 6. The B-mode points are generally consistent with zero across the plane and we checked that these are well-fit to a nearly flat line in all cases. The error bars are generally larger for the PSF-removed points than the SExtractor-only points without PSF-removal – as mentioned above, the process of removing the PSF increases the dispersion in shears by a large amount, and yet the central value of the average of the corrected shapes of the galaxies in any given bin is significantly closer to the actual input shear. This is indeed why the PSF is removed, though the uncertainty in shear spread after processing through the PSF-removal pipelines is always larger.

## 5 VARIATIONAL STUDIES

Having a simulated cluster in hand for which we know all the properties, we are able to do controlled studies from which we learn how the extracted  $\sigma_v$  varies with varying several types of cuts and weightings.

<sup>2</sup> Technically, this is because removing the PSF requires a step of division by the polarizability. However, the polarizability can approach zero for objects whose shape is badly determined, leading to the shear mathematically increasing to very large and unphysical values.

**Table 6.** Values of  $\sigma_v$  derived from the binned fits to the shear after the PSF has been removed, compared to the fit to the SExtractor-only ellipticities, with all objects from the same position-matched file (this corresponds to Fig. 8). The deviation is as described in Table 5, and for the  $\chi^2/\text{dof}$  the number of degrees of freedom is 11 because we restrict the fit range to less than the total extent of the image plane (see text). The central value from the shear output from each pipeline is within one sigma of the input, while it is over  $11\sigma$  away before PSF-removal.

File	Redshift	$\sigma_v$ (km/s)	$\sigma_{\sigma_v}$ (km/s)	$\chi^2/\text{dof}$	$\sigma$ Deviation
SExtractor Value LN PSF Applied File	0.84	954	26	12.9/12	11.4
Matched IMCAT Value LN PSF Removed File	0.84	1215	74	13.1/11	-0.5
Matched Shapelets Value LN PSF Removed File	0.84	1291	108	13.5/11	0.4
Non-matched IMCAT Value LN PSF Removed File	0.82	1224	59	10.2/11	-0.4
Non-matched Shapelets Value LN PSF Removed File	0.80	1373	102	20.2/11	1.2

### 5.1 Variation of results with type of redshift-correction

First, it is useful to investigate how the value we have assumed for  $\langle z_b \rangle$  of all the background galaxies in the single sheet approximation affects the resulting  $\sigma_v$ . In Fig. 9 we show the effect of varying the type of redshift correction on the objects for our reference file. The variation of both the IMCAT and Shapelets results are monotonic and linear downwards as  $\langle z_b \rangle$  is varied upward, with a nearly constant offset between each of results of each of the pipelines and the truth value, and the Shapelets value is always higher than the IMCAT one. We also note that the resultant  $\sigma_v$  is within one  $\sigma$  of the input value for single sheet approximation corrections from about  $\langle z_b \rangle = (\langle z_b^{\text{true}} \rangle - 0.1) \rightarrow \langle z_b^{\text{true}} \rangle$ .

### 5.2 Galaxy Cut Variation Studies

#### 5.2.1 Color Cuts

In order to most effectively remove the foreground and cluster galaxies when one has no redshift information on the galaxies, one generally makes a color cut on objects, as foreground and background galaxies are located in different loci of color space. By examining the distribution of the simulated objects, for which precise redshifts and magnitudes in various colors are known, it is possible to determine a color cut which will remove most of the foreground galaxies. For the reference file, we chose the simple  $r - i > 0.7$  cut shown in Fig. 10 (Cut A), and we describe in the same figure three other ways one might make this color cut. In Fig. 11, we show the effect varying the color cut has on the determination of  $\sigma_v$ . We see from this figure that the various possible ways of making color cuts have no dramatic effect on the  $\sigma_v$  values, except for Color Cut D for which the fit values for the truth and IMCAT deviate the most from the others. As in the previous section, the Shapelets results are consistently larger and both IMCAT and Shapelets generally track the truth value.

#### 5.2.2 Size Cuts

Various cuts on size are used to attempt to eliminate the error due to poor ellipticity and shear estimation. A larger object should in general have less error in its ellipticity and

shear estimation. The effect of various cuts on the FWHM are detailed in Fig. 12. We see mild variation in  $\sigma_v$  as a function of FWHM cut, with both the Shapelets and IMCAT  $\sigma_v$  tending slowly toward the input as smaller objects are cut out. This indicates that the better measurement of the shape of larger objects yields somewhat better final results. However, there is a tradeoff in that the error bars are also seen to grow steadily as the statistics are reduced (by about 49k to 37k galaxies from the mildest to strictest cut, a factor of about 25% fewer objects). Since magnification is not included in our simulation, we of course cannot quantify from these images yet further effects on the shear profile such as the effect of faint and small background galaxies becoming larger and magnified enough to be seen behind the cluster, also referred to as “lensing bias” (Schmidt et al. 2009a, Schmidt et al. 2009b).

#### 5.2.3 Noise Variation

Shapelets was not able to work on the High Noise files<sup>3</sup>, so the results in Fig. 13 are for IMCAT only. The Low Noise values have smaller error bars than the High Noise values, and this is only partly accounted for by the smaller number of objects in the HN images. In fact, the LN file has about 49k objects, and the HN one 23k, and the error bars on the extracted  $\sigma_v$  are 74 km/sec vs. 135 km/sec, where if we scaled just by statistics on the LN error we would obtain 108 km/sec. Thus, the HN error is a factor of about 25% higher than just statistical scaling, indicating that the higher noise has led to a wider spread in the shear estimates of the objects.

From this we see that higher noise is harmful to profile extraction not only for suppressing statistics, but intrinsically in worsening shape estimation of objects.

<sup>3</sup> This is regularly seen, and occurs essentially because IMCAT needs only a few parameters to describe the shape of the ellipse that circumscribes an object, while Shapelets aims to extract the total shape information of an object into a coefficient basis, and will fail more often in low S/N situations where the edges are less well-defined.

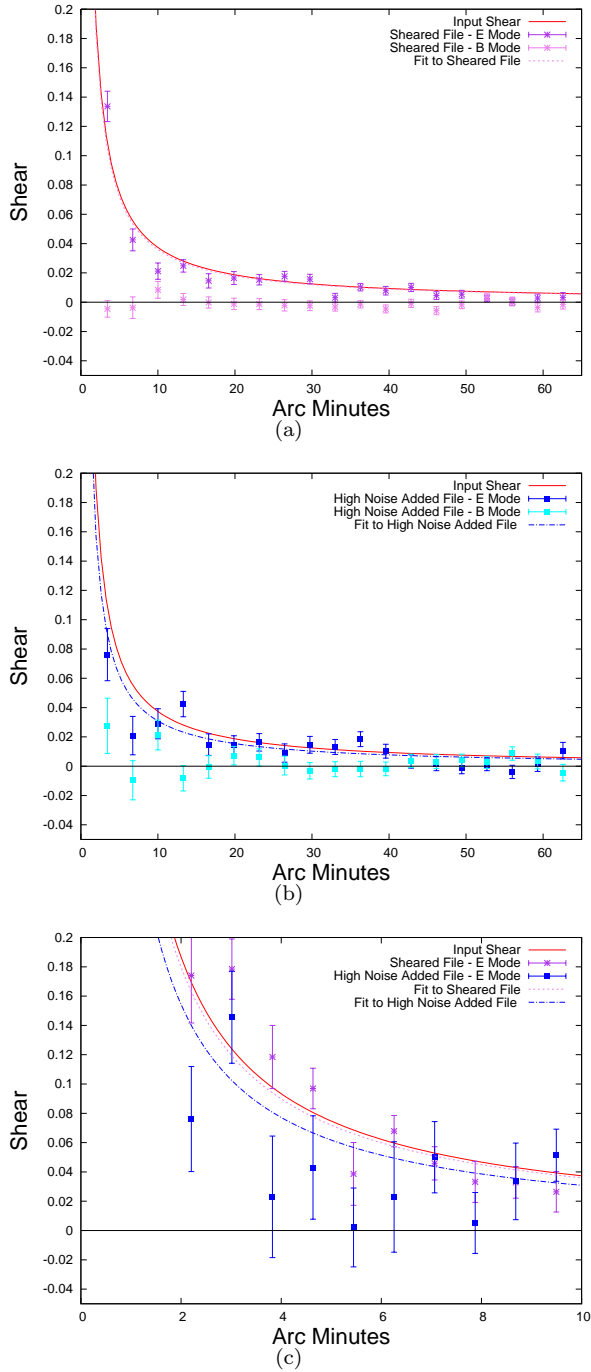


**Figure 7.** SEExtractor ellipticity annular profile averages corresponding to the numerical outputs of just two files from Table 5: the no noise sheared file (row 2 of the Table), and the sheared file with high noise (row 3 of the Table). The label “Shear” on the y-axis is actually simply the mean tangential galaxy ellipticity. The red solid line shows the SIS profile for the input value of  $\sigma_v$ , while the points show the E- and B-mode profiles averaged in annular bins from the center of the cluster to the edge of the image. Error bars here and in all binned profile plots are the rms spread in shear divided by  $\sqrt{N}$ , where  $N$  is the number of galaxies in each annular bin. (a) Shows the result from the no noise sheared file (28.0k objects), (b) Shows the result from the high noise sheared file (43.6k objects), and (c) shows a zoom in of both, with only the E-mode data points shown.

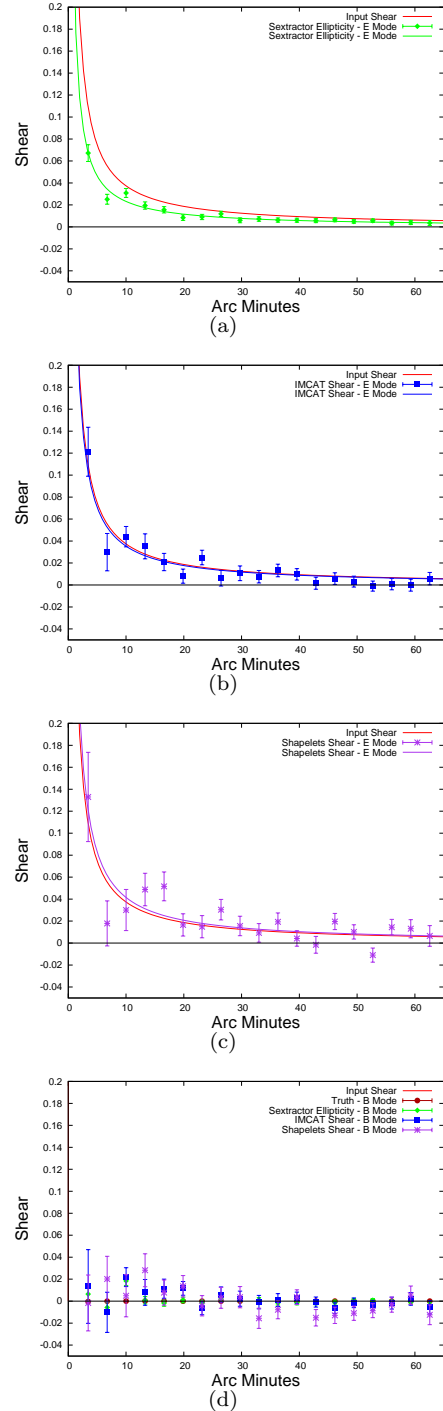


**Figure 8.** Profiles for SEExtractor and PSF-removed files compared to the input for the entire image plane from the reference file (see Sec. 4.3.2) – i.e. the Low Noise file with foreground galaxies removed by color cut, all galaxies redshift-corrected to  $z = 0.84$  (see Sec. 5.2.1), and all objects position-matched between the IMCAT and Shapelets files. This results in a single file of 49.2k objects. The fit profiles correspond to the values in Table 6. The red solid line corresponds to the input value in all cases, and also shown are the binned data points and the fit profile to the unbinned data. Shown are the values for (a) SEExtractor ellipticity (b) PSF-removed IMCAT shear and (c) PSF-removed Shapelets shear.

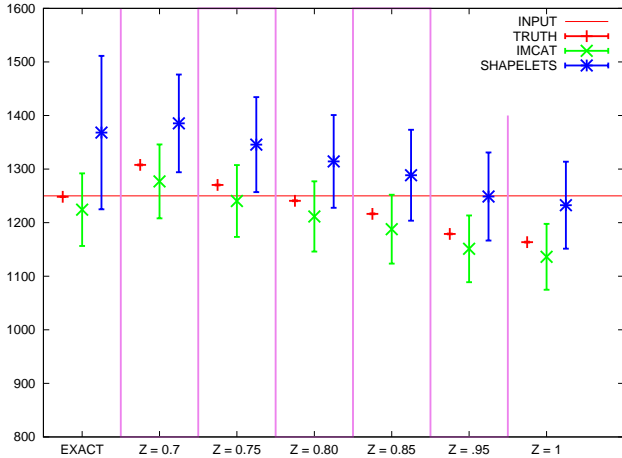
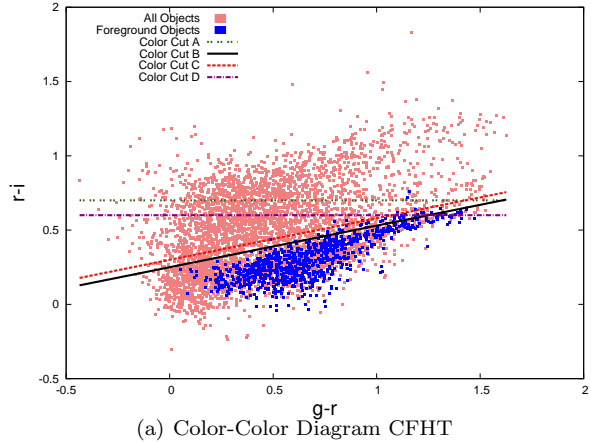


**Figure 9.** Variation of  $\sigma_v$  with differing ways to apply a redshift correction to the background objects. The leftmost column shows the effect of using the exact correction for each object using its known redshift. The following columns show the effect of using the single sheet approximation with the objects fixed to varying redshifts. The actual average redshift of all the background galaxies is  $\langle z_b^{true} \rangle = 0.84$ . The red crosses represent the effect of doing the correction on the truth values of the shear for each object, the green x's the same on the IMCAT values of the shear for each object, and the red \*'s the same on the Shapelets values of the shear for each object.

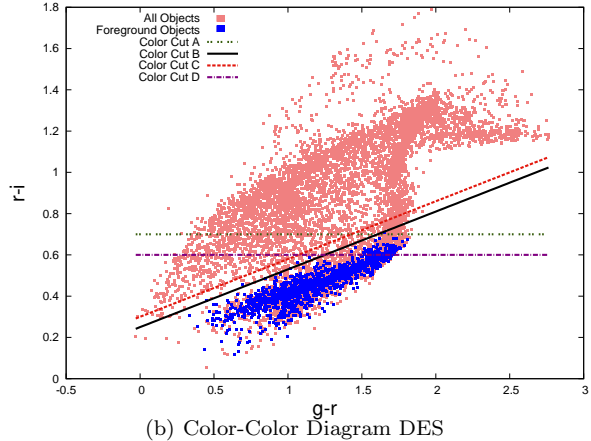
### 5.3 Bootstrap Results

As a simple test to verify that the differences in the central values for  $\sigma_v$  were significant for the cut variations discussed above, we did a bootstrap test for two different cuts (varying the galaxy size cutoff) in one pipeline (IMCAT). To do this, we used one example original file to first make 1000 bootstrap samples (choosing 21k out of 21k galaxies randomly, so that some galaxies were not chosen, and others were picked more than once). We then applied the two differing cuts on each sample, creating a pair of files for each of the samples. Next, we extracted the two  $\sigma_v$  values for each sample pair, and took the difference of these values. Finally, we compared the width of the distribution of this difference to that of the  $\sigma_v$  distribution of the original 1000 file bootstrap sample. We found that the former was smaller by more than a factor of five, indicating a strong correlation between each sample pair – i.e. the cuts were affecting each bootstrap sample in the same direction. This indicates that the observed differences are in fact significant in this case.

We further probed this by evaluating a standard correlation coefficient test on the samples, and found a 98% correlation in the results in the case where the cuts were made on the same exact samples as above. This fell to an 11% correlation in bootstraps where the pair of cuts were not made on random files in the ensemble. This further indicates that the differences between the central values in the samples after cuts are indeed significant as we have been assuming previously.



(a) Color-Color Diagram CFHT



(b) Color-Color Diagram DES

**Figure 10.** Color-Color Plots for the Low Noise file with foreground galaxies. For CFHT, color and redshift information is from observations, while for our simulated image, the color and redshift information is obtained from a match to the truth files, for which such information is available (see Sec. 2.3). “Color Cut A” selects the objects for which  $r - i$  is greater than 0.7. “Color Cut B” selects the objects for which  $r - i$  is greater than  $(g - r) \times 0.28 + 0.25$ . “Color Cut C” selects the objects for which  $r - i$  is greater than  $(g - r) \times 0.28 + 0.3$ . “Color Cut D” selects the objects for which  $r - i$  is greater than 0.6. Note that though the Color-Color diagrams for CFHT and DES look fairly different, the same color cuts do seem to have similar effects in how much foreground contamination is removed for both of them.

## 6 CONCLUSION

We have run two independent weak lensing analysis pipelines on a suite of realistic simulated galaxy cluster images created in the framework of the simulation tools developed by the Dark Energy Survey. This simulation contains noise, foreground objects, and a PSF which varies both in FWHM and ellipticity. Both pipelines give results that are within the one-sigma error bars of the input value using the same processing that would be applied to real data. Thus, our analysis of this DES cluster simulation demonstrates that both the IMCAT and Shapelets pipelines are able to reproduce the input singular isothermal sphere  $\sigma_v$  in a realistic simulation, suggesting that current weak lensing tools are accurate enough for extracting the shear profile of massive

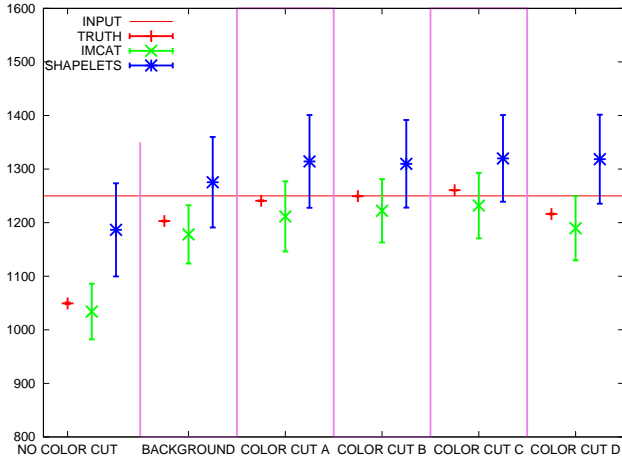


**Figure 11.** Variation of  $\sigma_v$  with varying color cuts. Symbols are as in Fig. 9, and cut labelling is as in Fig. 10. All objects are corrected to the single sheet approximation value of  $\langle z_b \rangle = 0.84$ . In the column labelled “Background” we have used the truth information on the redshift of each object to select all the true background galaxies.

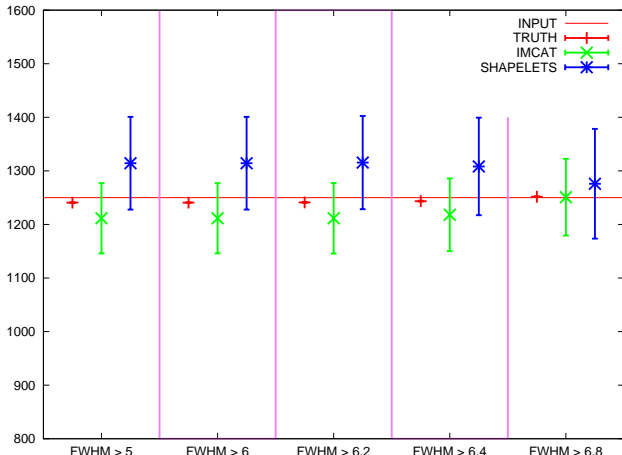


**Figure 12.** Variation of  $\sigma_v$  for various FWHM Cuts. Symbols are as in Fig. 9. All objects are corrected to the single sheet approximation value of  $\langle z_b \rangle = 0.84$ . The cuts range from “no cut” in the leftmost panel (i.e.  $\text{FWHM} > 5.0$  pixels, as is already done for the initial galaxy selection) to  $\text{FWHM} > 6.0, 6.2, 6.4, 6.8$  pixels in the following four panels.

clusters in upcoming large Stage III (Albrecht et al. 2006) photometric surveys such as DES.

These new simulations are quite a bit more realistic than the STEP simulation images to test pipelines for cluster weak lensing profile extraction accuracy, since with real data one must in general remove a PSF that varies in size and ellipticity across the focal plane. With this simulation it was possible to also test more realistic galaxy selection cuts such as those made on color and size, as well as vary the fit limits and star selection, and demonstrate that the pipelines were able to handle these different choices robustly. It seems as though IMCAT can handle images with a high

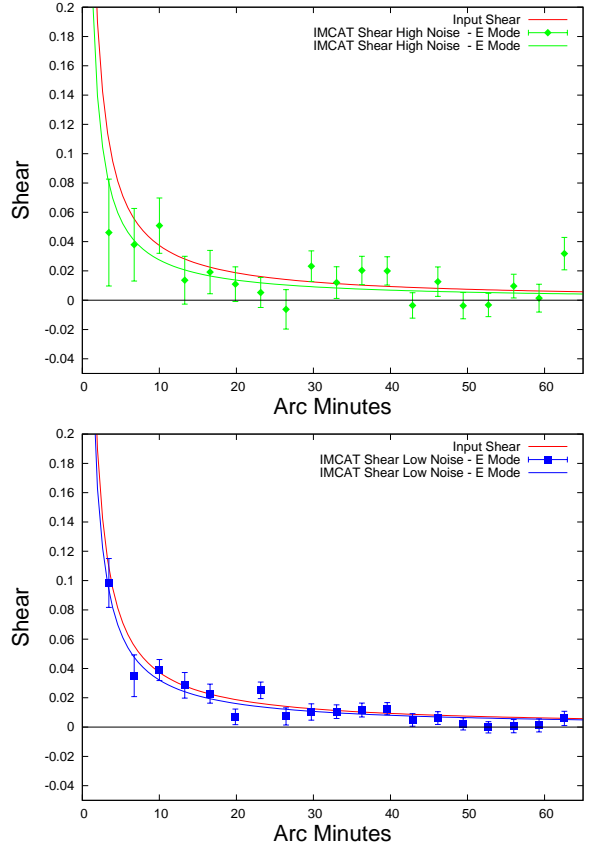


**Figure 13.** Fit profiles and binned points for two levels of noise. All objects for the (a) High Noise file are corrected to the single sheet approximation value of  $\langle z_b \rangle = 0.64$  (23.1k objects), All objects for the (b) Low Noise file are corrected to the value of  $\langle z_b \rangle = 0.84$  (49k objects). The  $\chi^2_{\text{dof}}$  is 13.2/12 for the LN file, and 8.2/12 for the HN one. Note the larger error bars on the HN points (see text in Sec. 5.2.3).

level of noise more robustly than Shapelets, although both pipelines performed better on images with a low level of noise. While this indicates that Shapelets may not be indicated for future rapid cadence surveys, we do point out we have only worked thus far with our implementation and configuration of the method and code.

Using both of these independent pipelines and potentially others in parallel on the same future cluster data samples will provide an internal crosscheck which will give confidence on shear estimates and masses extracted from cluster weak lensing analyses. We will follow this study with future analyses on suites of multiple weakly lensed cluster images with differing noise levels with different shear profiles (such as NFW) to do statistical tests on the pipelines. The dominant errors are from noise and galaxy statistics, thus it is important to have a large enough galaxy sample in an image with as low as possible noise properties in order to get the optimal shear profile.

We are making the suite of images used in this analysis publically available for others to analyze at <http://ccapp.osu.edu/DEScluster>.

**ACKNOWLEDGMENTS**

The simulated images used in this study are based on the DES mock galaxy catalog created by M. Busha and R. Wechsler, and we fully express our appreciation to them for being able to use these catalogs.

We would like further to very much thank D. Applegate, J. Beacom, J. Berge, G. Bernstein, S. Bridle, J. Cohn, D. Clowe, T. Eifler, G. Evrard, J. Frieman, S. Habib, B. Jain, M. Jarvis, C. Kochanek, K. Kuehn, S. Kazantzidis, A. Leauthaud, R.J. Massey, T. McKay, R. Nakajima, C. Orban, B. Ragazzone, B. Rowe, E. Sheldon, A. Slosar, G. Steigman, M. White, H. Yan, and A. Zentner for many helpful discussions, pointers and readings.

**REFERENCES**

Abbott, T. et al., The Dark Energy Survey Collaboration, modified version of White Paper submitted to the Dark Energy Task Force [arXiv:astro-ph/0510346]  
 Albrecht et al., Dark Energy Task Force Report, 2006 [arXiv:astro-ph/0609591]  
 Bacon, D., Refregier, A., Clowe, D., Ellis, R. Volume 325, Issue 3, Pages 1065-1074 [arXiv:astro-ph/0007023]  
 Bartelmann, Matthias and Schneider, Peter, 2001, Phys. Rept., [arXiv:astro-ph/9912508]  
 Bernstein, G.M. and Jarvis, M., 2002, [arXiv:astro-ph/0107431]  
 Bertin, E., Arnouts, S., 1996, Astronomy and Astrophysics Supplement, 117,393  
 Blanton, M. R., et al. 2003, ApJ, 592, 819  
 Bridle, S., et al. Annals of Applied Statistics 2009, Vol. 3, No. 1, 6-37 [arXiv:0802.1214]  
 Colberg, J. M., et al. 2000, MNRAS, 319, 209 [arXiv:astro-ph/0005259]  
 Gerdes, D.W., et al. 2009, submitted to Astrophys.J. [arXiv:0908.4085]  
 Heymans, C., et al. 2005, MNRAS 368 1323 (STEP1) [arXiv:astro-ph/0506112]  
 Hoekstra, H., Franx, M., Kuijken, K., and Squires, G. (1998). Weak Lensing Analysis of CL 1358+62 Using Hubble Space Telescope Observations <http://adsabs.harvard.edu/abs/1998ApJ...504..636H>. ApJ 504, 636. [arXiv:astro-ph/0810360v1]  
 B. Holwerda, 2005, [arXiv:astro-ph/0512139v1]  
 K. Honscheid, et al. 2008, [arXiv:astro-ph/0810360v1]  
 Kaiser, N., Squires, G., & Broadhurst, T. 1995, ApJ, 449, 460  
 Luppino, G. and Kaiser, N. Astrophys.J. 475 (1997) 20 [arXiv:astro-ph//9601194v1]  
 Monet, D., et al. 2003, AJ, 125, 948  
 Massey, R. et al. 2007, MNRAS 376 13 [arXiv:astro-ph/0608643v2]  
 Massey, R. et al. 2007, MNRAS 380, Issue 1, pp. 229-245 [arXiv:astro-ph/0609795]  
 Narayan, R. and Bartelmann, M. , 1996 , [arXiv:astro-ph/9606001v2]  
 Peacock, J.A., Schneider, P., Efstathiou, G., Ellis, J.R., Leibundgut, B., Lilly, S.J., Mellier, Y.; ESA-ESO Working Group on "Fundamental Cosmology" . Tech. Rep. Oct. [arXiv:astro-ph/0610906]

Refregier A. 2003, MNRAS 338 35 [arXiv:astro-ph/0105178v1]  
 Scoville, N., et al. 2007, ApJS, 172, 1  
 Schmidt, F., Rozo, E., Dodelson, S., Hui, L., Sheldon, E., Phys. Rev. Let. 103, 051301 (July 2009) [arXiv:0904.4702]  
 Schmidt, F., Rozo, E., Dodelson, S., Hui, L., Sheldon, E. , Journal-ref: Astrophys.J.702:593-602,2009 [arXiv:0904.4703]  
 Wechsler, R et al. in preparation.  
 Wechsler, R, "Interpreting SDSS Cluster Masses and Abundances with Mock Catalogs" in Clusters of Galaxies: Probes of Cosmological Structure and Galaxy Evolution, from the Carnegie Observatories Centennial Symposium. Carnegie Observatories Astrophysics Series. Edited by J.S. Mulchaey, A. Dressler, and A. Oemler, 2004. Pasadena: Carnegie Observatories.